Spring 2024

Numerical Study in Wind Energy Extraction from Controlled Limit-Cycle Oscillations in Modified Glauert Airfoil

Ethan L. Deweese
Embry-Riddle Aeronautical University, deweesee@my.erau.edu

Scholarly Commons Citation

Deweese, Ethan L., "Numerical Study in Wind Energy Extraction from Controlled Limit-Cycle Oscillations in Modified Glauert Airfoil" (2024). *Doctoral Dissertations and Master's Theses*. 805.
https://commons.erau.edu/edt/805

NUMERICAL STUDY IN WIND ENERGY EXTRACTION FROM CONTROLLED LIMIT-CYCLE OSCILLATIONS IN MODIFED GLAUERT AIRFOIL

By

Ethan DeWeese

A Thesis Submitted to the Faculty of Embry-Riddle Aeronautical University
In Partial Fulfillment of the Requirements for the Degree of
Master of Science in Aerospace Engineering

May 2024
Embry-Riddle Aeronautical University
Daytona Beach, Florida

NUMERICAL STUDY IN WIND ENERGY EXTRACTION FROM CONTROLLED LIMIT-CYCLE OSCILLATIONS IN MODIFED GLAUERT AIRFOIL

By

Ethan DeWeese

This Thesis was prepared under the direction of the candidate's Thesis Committee Chair, Dr. Vladimir Golubev, Department of Aerospace Engineering, and has been approved by the members of the Thesis Committee. It was submitted to the Office of the Senior Vice President for Academic Affairs and Provost, and was accepted in the partial fulfillment of the requirements for the Degree of Master of Science in Aerospace Engineering.

THESIS COMMITTEE

Chair, Dr. Vladimir Golubev	Member, Dr. William MacKunis
Member, Dr. Reda Mankbadi	
Graduate Program Coordinator, Dr. Hever Moncayo	Date
Dean of the College of Engineering, Dr. James W. Gregory	Date
Associate Provost of Academic Support, Dr. Kelly Austin	Date

ACKNOWLEDGEMENTS

I would like to thank my committee member Dr. William MacKunis and Dr. Reda Mankbadi for their guidance through the completion of this thesis, and my committee chair and advisor, Dr. Vladimir Golubev, for the opportunity to work on this project.

To my students in the wind tunnel laboratory, you have taught me as much as I have hoped to teach you. Thank you to my friends in the Aerospace Engineering Department for making the long days a little shorter. For my parents and their unwavering support to make this journey possible I will always remember.

To Lap Nguyen, whose work this thesis is a spiritual successor, thank you for the time out of your busy schedule and patience to bring me up to speed. I would also like to acknowledge Likhit Mohanranga and Erik Vataker, for their help in data collection of high- and low-fidelity results, respectively.

Experimental Data was provided by Dr. Oksana Stalnov, Ron Efrati and Shay Monat, Technion-Iseral Institute of Technology. This work was completed in part with funding from NSF-BSF award #1809790.

ABSTRACT

Typically, wind energy harvesting technology employs wind turbines. Towards the goal of meeting increasing energy needs with renewable energy sources a novel wind energy harvesting scheme is considered, utilizing a modified Glauert (MG) airfoil experiencing aeroelastic limit cycle oscillation (LCO) from which energy may be extracted. Synthetic jet actuators (SJA)s are used along with the unique geometry of the MG airfoil to control flow separation and amplify the LCO and energy generation potential of the system. The discussed wind energy harvesting scheme could provide flexibility in allowing installations previously unsuitable to wind turbines due to geometric or low wind velocity constraints. Without SJA control at 7 m/s wind speed, predicted net power output is 2.35 W per meter span. With SJA control, this increases to 4.05 W.

Towards the study of an MG airfoil under LCO, this thesis evaluates variable-fidelity numerical schemes. A high-fidelity implicit large eddy simulation (ILES) solver FDL3DI is employed to directly compute the flow field around the moving airfoil, and especially the effects of SJA control. For a low-fidelity tool, the panel method solver with boundary layer prediction XFOIL is used. Both numerical tools compare well to steady-state experimental results.

The MG airfoil geometry exhibits LCO below the velocities predicted by inviscid unsteady thin airfoil theory (UTAT) due to separation near the rear of the airfoil, including with only 1 degree of freedom (DOF). Both simple open- and closed-loop controllers show success in amplifying plunging LCO motion by activating SJAs with the natural frequency of plunging. When the low fidelity tool is complete, it can be used for fast structural, control, and geometric optimization to further increase the energy harvesting potential of the system.

TABLE OF CONTENTS

LIST OF FIGURES

Figure Page

LIST OF TABLES

Table Page

NOMENCLATURE

AoA	Angle of Attack
DOF	Degree(s) of Freedom
HPC	High-Performance Computing
ILES	Implicit Large Eddy Simulation
LCO	Limit Cycle Oscillation
LE	Leading Edge
MG	Modified Glauert
MIT	Massachusetts Institute of Technology
SJA	Synthetic Jet Actuator
TE	Trailing Edge
UTAT	Unsteady Thin Airfoil Theory

1 Introduction

With a more sustainable future in mind, electrical power production is increasingly switching to renewable forms of power, with solar and wind accounting for 49% and 22%, respectively, of new installed capacity in the United States in 2022 [1], bringing the nameplate wind power capacity to 144 GW in 2022, shown in Figure 1.1. This growth is in large part to wind turbines increasing in height and rotor diameter, aiming to access higher wind speeds utilizing the higher tower height [1]. While specific power, measured in watts per meter squared of rotor area, is on the decline in the US, wind power installations are still utilizing significant wind speeds, with 2022 installations having an average wind speed of 8.3 m/s (18.6 mph) at 100 m (328 ft) altitude [1].

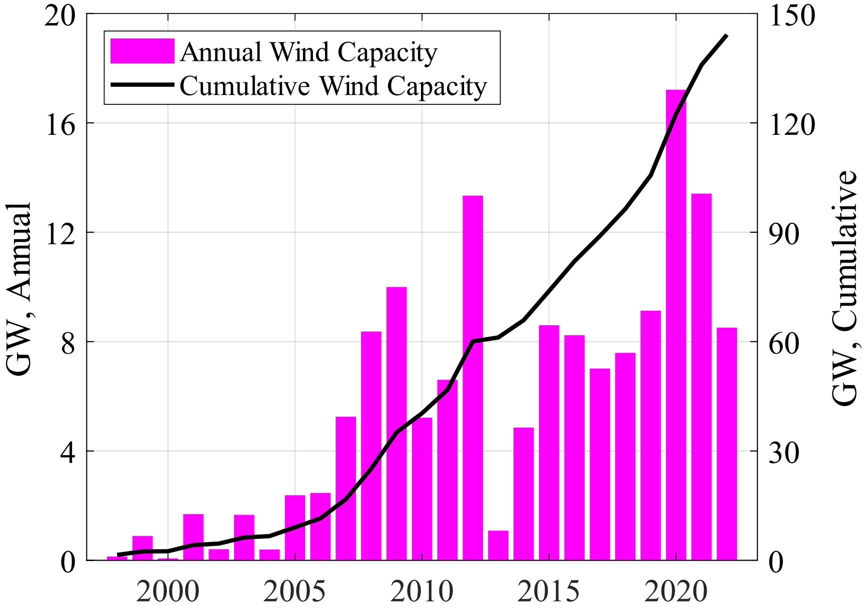

Figure 1.1 Cumulative and annual land-based wind energy growth in the US [1].

Focusing on record-breaking turbines in mass installations ignores the collective work that can be done by many smaller projects. Residential renewable energy generation is dominated almost entirely by photovoltaic solar, although wind turbines on the scale of powering a single residential household do exist. However, the smaller rotor of such a turbine limits its captured volume of air, and the shorter tower lowers the wind speed available to the already small rotor, both reducing power capacity. Thus, along with issues of visual impact, small-scale wind power has failed to take off. This is not to say that small scale wind power has no potential. A change in configuration away from the classic turbine poses potential to reinvigorate small wind energy harvesting.

1.1. Aeroelastic Flutter

Aeroelasticity concerns the effects of aerodynamic forces on an elastic structure [2]. Beginning with the structural response, the typical model follows Hooke's law:

$$F = -kx \tag{1.1}$$

Where the force response, F, is directly proportional by the stiffness constant, k, and opposite in direction to the displacement from the neutral position, x (and in a rotational sense, torque,τ , and angle, θ). The stiffness of the structure depends on its geometry and material, and the linear relationship holds for quasi-steady small deflections. The aeroelastic model considering inertial effects of non-vanishing motion is discussed in Section 2.3.

Aeroelasticity can be studied in the sense of finding stable configurations for designs that should be steady in any wind, such as buildings or bridges. Alternatively, the structure can be intentionally sprung for stable aeroelastic motion. Here, consider an airfoil that is elastically mounted in the vertical and pitch directions, shown in Figure 1.2. The aerodynamic performance depends on airfoil geometry but will follow the general trend show in Figure 1.3; a linear increase in lift until some angle of attack were flow on the upper surface of the airfoil will separate and the airfoil will stall with an associated decrease in lift. Overall, at low flow velocities, the aerodynamic forces are less the then restoring structural forces, so the system is stable, and any positional disturbance reduces over time. At some critical flow velocity, the system is neutrally stable and an initial disturbance results in a steady oscillation, known as flutter. As flow velocity increases the magnitude of oscillation increases.

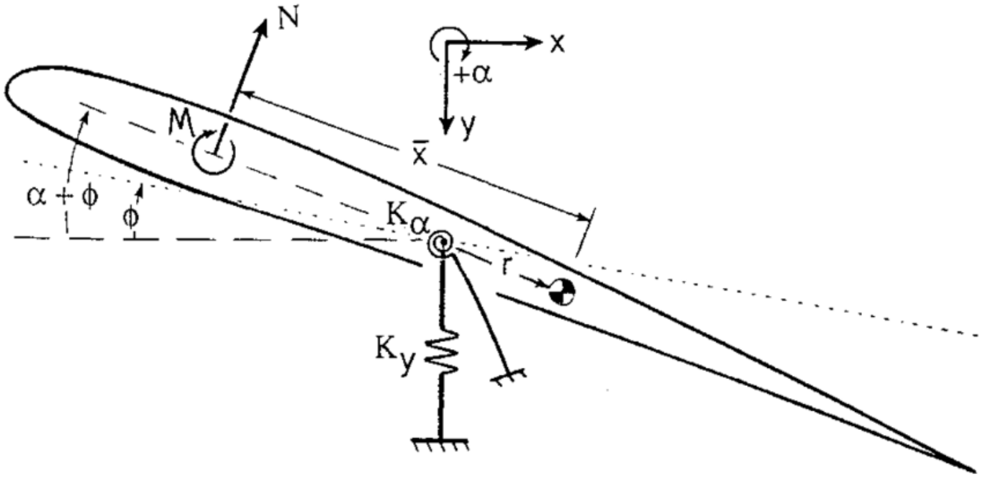

Figure 1.2 An airfoil elastically mounted in the vertical and pitch axis [3]. Flow enters horizontally from the left to right.

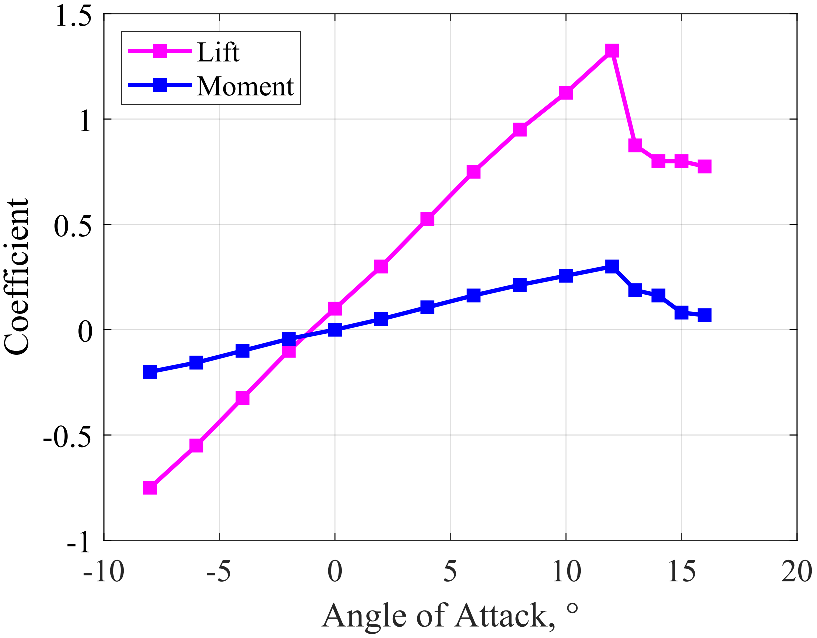

Figure 1.3 Lift and quarter-chord moment coefficient curves for the NACA 1408 airfoil [4].

Limit cycle oscillation (LCO) occurs in a system such as a fluttering airfoil due to nonlinearities. A system with a stable limit cycle oscillation has an oscillatory mode of a frequency determined by the system nonlinearity and nearly constant amplitude not dependent on the input disturbance [5]. For a flutter-based wind energy harvester, LCO can be caused by nonlinearities due to aerodynamic, structural, or generator properties. The aerodynamic nonlinearity is usually stall, where the lift and pitching moment reach a maximum. Structural nonlinearities are non-zero higher order stiffness terms, such as $k_{\alpha,3}\alpha^3$, as discussed in section 2.3. Generator nonlinearities vary based on the type and set-up of generator.

1.2. Flutter-based Wind Energy Harvesting

LCO- and flutter-based wind energy harvesting has been studied with many configurations. Broadly, they can be categorized based on the aerodynamic configuration and electrical generator. Reviews by Nabavi et. al. [6], Li et. al. [7], and Ma et. al. [8] summarize recent developments.

1.2.1. Electricity Generation Methods

Most conventional in terms of wind turbines and classical power plants is electromagnetic electricity generation, where the relative motion between a magnetic field and conductor induces a current in the conductor. While in large installations this motion is rotary, flutter-based wind harvesting utilizes the oscillating linear component of flutter by attaching the magnet or coil to the moving component while holding the other coil or magnet stationary. One such implementation [9], places the magnet in the middle of a tensioned membrane, but various airfoil- or blunt-body-based configurations are possible.

The other common generator is piezoelectric. The piezo electric effect describes materials where deformation is related to a voltage. When a piezoelectric material is deformed, a voltage is experienced, and vice versa. The piezoelectric material is bonded to some vibrating section of the flutter-based wind energy harvester, so the vibration can continuously deform the piezoelectric material and generate electricity over time. Compared to electromagnetic wind energy harvesters, piezoelectric devices can have higher power densities [10], although due to the lower resistance of a conductive coil, electromagnetic devices can produce higher currents [9].

Another novel method of electricity generation is triboelectric. The method of electricity generation is the direct transfer of electrons from one place to another, accomplished with a thin fluttering membrane situated between two plates [11], [12]. The alternating contact between the membrane and each place creates a voltage across the device.

1.2.2. Physical configurations

The general concept of an elastic device with aerodynamic properties such that it experiences flutter can take many forms. One major line of development utilizes vortex shedding from blunt bodies to excite the system. The blunt body may be attached to a flexible beam, fixed at one end, such that the system's natural frequency aligns with the vortex shedding frequency [8]. The piezoelectric material is then attached to the flexible beam, as described in Figure 1.4.

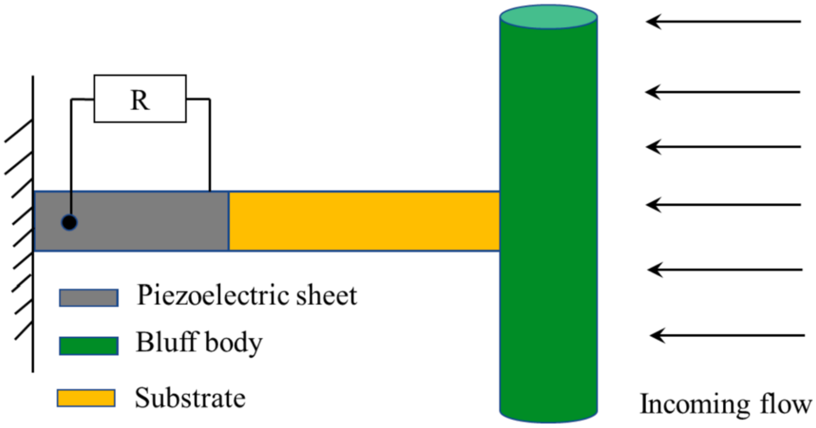

Figure 1.4 Schematic of bluff body wind energy harvester [8].

An airfoil-based flutter wind energy harvester can be of similar configuration, replacing the bluff body with an airfoil mounted so that it is also free to pitch relative to the end of the beam, giving the airfoil freedom in 2 degrees of freedom. Similar motion could be accomplished with an airfoil mounted with a bearing to linear rails, so that the plunging motion is strictly vertical rather than an arc with a radius equal to the length of the beam.

Especially for low power applications, a tensioned band can act as both the aerodynamic and structural component, as in Figure 1.5.

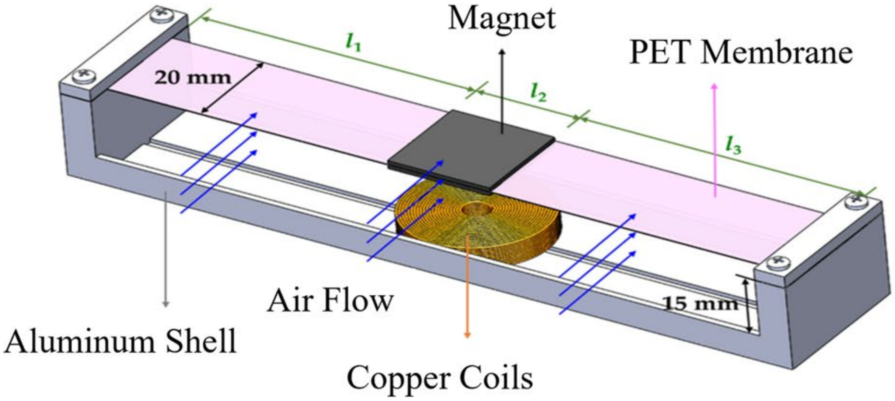

Figure 1.5 Schematic of band-based flutter wind energy harvester [7].

1.3. Airfoil Selection

The airfoil requirements for this project diverge from the common lines of airfoil development. Typical subsonic airfoil design focuses on efficiency or maximum lift coefficient, where separation is to be avoided. Here, separation is to be controlled to increase aerodynamic forces on the oscillating airfoil and increase the amplitude of oscillation. Thus, an ideal airfoil would have large naturally separated regions such that a small control input has a large destabilizing effect on the airfoil, increasing energy harvesting potential.

1.3.1. Glauert GLAS Airfoils

The lineage of the current airfoil starts with airfoil geometries published by Glauert in 1945 [13]. Glauert's GLAS I – GLAS IV airfoils were designed for high lift coefficient over a large range of angles of attack, accomplished with a suction slot around 70% x/c on the upper surface. The airfoils were designed based on a desired surface velocity profile using an exact potential flow design method [14] set by Lighthill [15], where the suction slot creates the surface velocity discontinuity required. The airfoils, as shown in Figure 1.6, are to maintain a laminar flow across as much of the operating range as possible and have high thickness to maximize internal volume. The step around 70% x/c is an artifact of the logarithm spiral required by the design method to match the discontinuous surface velocity profile.

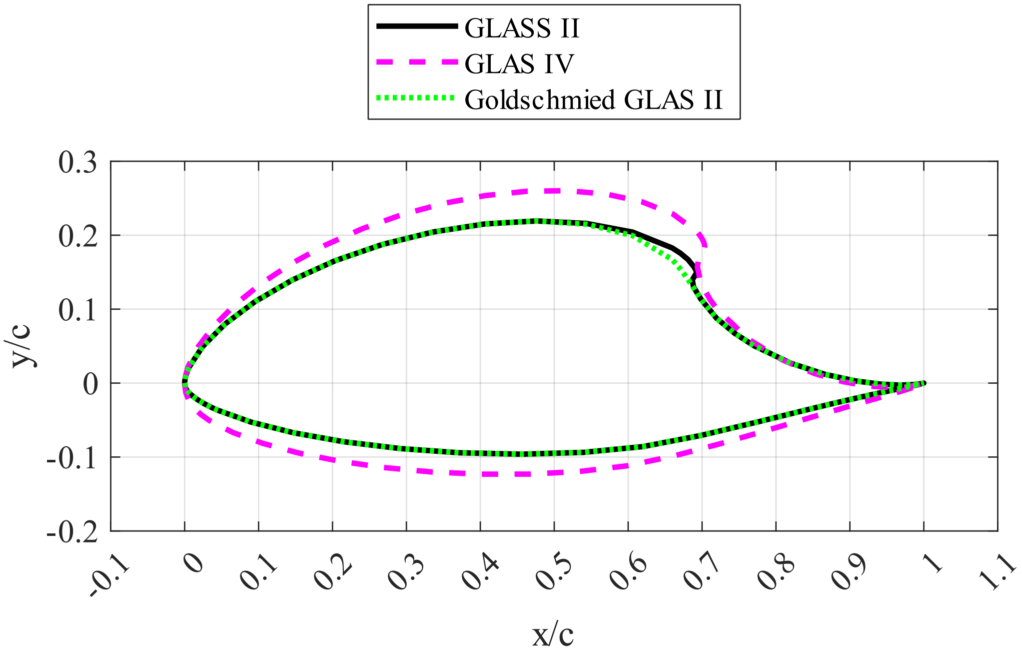

Figure 1.6 GLAS II and GLAS IV airfoils developed by Glauert [1] and modified GLAS II airfoil proposed by Goldschmied [16].

1.3.2. Modified Glauert (MG) Airfoil

The Glauert airfoils have been investigated several times since their development. Goldschmied in 1990 presented a "Thick-Wing Spanloader" concept where the large internal volume of a modified GLAS II airfoil was to become the cargo bay of a flying wing aircraft [16]. The airfoil maintains the suction slot near its original position, but the step associated with the logarithm spiral has been faired over, also plotted against the original in Figure 1.6. Saeed and Selig in 1996 present an updated design methodology for slot suction airfoils to explicitly include suction at the slot, improving Glauert's and Lighthill's original methods of prescribing a discontinuous velocity profile [17].

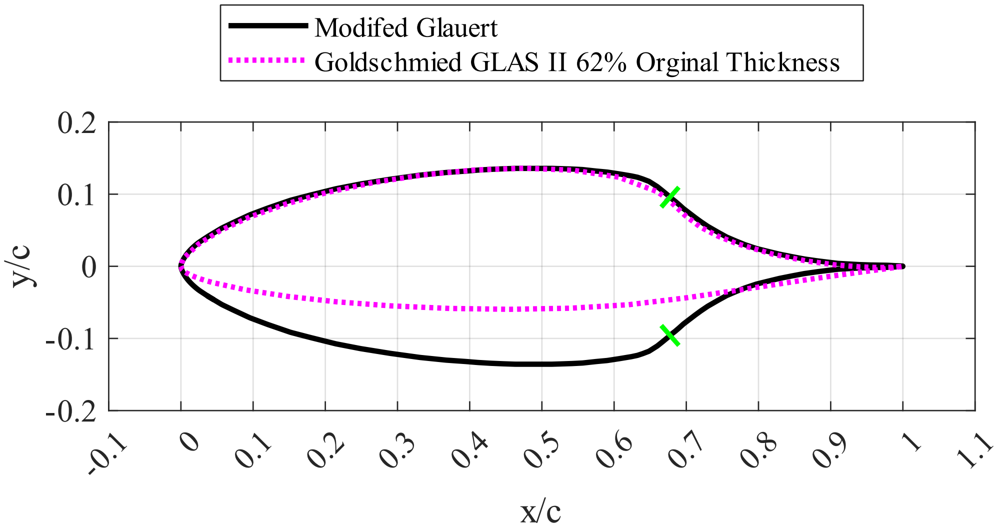

Figure 1.7 MG airfoil with green dashes at 68% chord indicating position of embedded SJAs. The thinned Goldschmied GLAS II type airfoil is plotted for comparison.

Seifert and Pack in 2012 [18] are the first to present the current modification of the Glauert airfoil with experimental studies of active flow control on one half the airfoil as a wall-mounted hump. The step around the suction slot is faired like Goldschmied's version, and the thickness of the GLAS II is reduced to 62% of its original thickness. Work continued, [19] and [20], on active control on the asymmetric modified Glauert airfoil. The current airfoil, in Figure 1.7, takes the upper surface of Seifert's airfoil and mirrors it, creating the symmetrical modified Glauert airfoil (henceforth modified Glauert or MG airfoil), as to allow control during both directions of oscillation. The MG airfoil has a maximum thickness of 27% between 46% and 51% x/c. Synthetic Jet actuators (SJAs) are implanted at 68% x/c on both surfaces, near the point of flow separation.

1.4. Synthetic Jet Actuators (SJAs)

Towards increasing the potential energy extraction of the oscillating airfoil, especially at low freestream velocities, a cost effective and energy efficient actuator is desired. To exploit the natural separation of the MG airfoil, SJAs are implanted in the airfoil surface near the flow separation point. Here, they can work to selectively reattach the flow on one surface, unbalancing the forces on the symmetric airfoil and inducing motion.

SJAs are zero net mass flux devices, typically a piezoelectric element connected to a diaphragm in a cavity below the surface of the airfoil [21], as shown in Figure 1.8. The piezoelectric element, diaphragm, cavity dimensions, and orifice form a resonant system producing a sinusoidal in time velocity profile out of the orifice:

$$U_{SJA}(t) = U_{SJA,max} \cdot \sin(\omega t) \qquad (1.2)$$

The SJA can act at a point, with a circular diaphragm and orifice, or be extended along one axis to create a line jet. In this research, SJAs are implanted on both upper and lower airfoil surfaces, with the orifice from 67.5% to 68% x/c. They oscillate at 200 HZ, with a jet velocity amplitude of ± 13.5 m/s. As the CFD simulation in this work was conducted in 2D, the jet is analogous to a continuous jet across the span of the wing. Later, evaluating the required percentage of span covered by SJA could decrease the required jet power, hence increasing the net available power of the wind energy harvester.

SJAs offer several advantages over other actuators. A conventional deflection control surface on the MG airfoil would be operating in a separated region of flow, and thus have reduced authority. Also, mechanical actuation is more complex and does not utilize the unique geometry of Glauert-type airfoils. The MG airfoil lineage is of "slot-suction" airfoils, where a slot (typically around 70% x/c) is connected to a blower in suction to reattach flow. Typically, the blower exhaust would be directed out of the trailing edge. While this does utilize the geometry of the MG airfoil, mechanical complexity remains, and now actuation speed and energy expense of the blower become limitations. So, SJAs retain some of the flow control authority benefits of slot suction with a simpler mechanical design and fast response time for controlled oscillation.

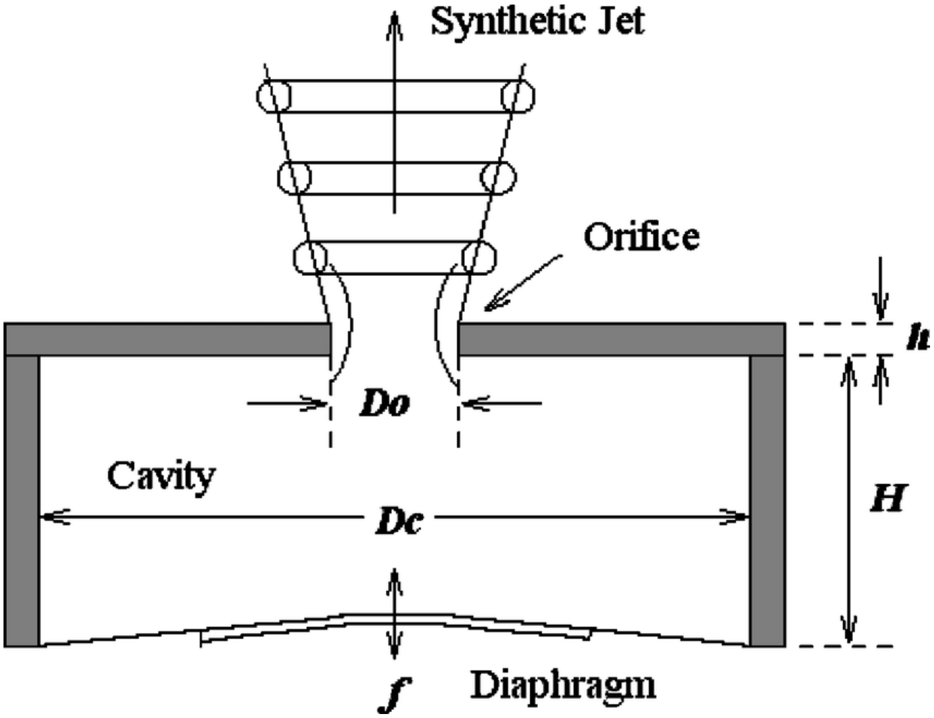

Figure 1.8 A Synthetic Jet Actuator [22].

2 Methodology

Two numerical methods for the flow solution were employed. The high-fidelity approach was the implicit large eddy simulation (ILES) tool FDL3DI, originally developed at the Airforce Research Laboratory (ARFL), and XFOIL, a panel method with boundary layer correction, was developed at MIT. Steady state solutions are validated against experimental pressure distribution, and both flow solutions can integrate with the quasi-linear aeroelastic model derived by Berggren to obtain the oscillation response of the airfoil with and without control inputs.

2.1. High-Fidelity Solver

The flow around the MG airfoil is characterized by separated regions downstream of the corner on each surface of the airfoil. In addition, SJAs control the airfoil by impinging on the boundary layer. Thus, a CFD solution needs sufficient resolution down to the boundary layer to accurately determine the control authority of SJA implementations.

Based on previous work, Flight Dynamics Laboratory Three-Dimensional Implicit (FDL3DI), a Fortran-based ILES solver developed at the ARFL is employed. FDL3DI [23] solves the unsteady compressible Navier-Stokes problem with 6th order accuracy in space and 2nd order accuracy in time with compact finite differencing on a structured grid and sub iterations between each time step.

The grid is 1363 points along the airfoil surface, 814 points radially outward, and 3 points spanwise to accommodate the points required for FDL3DI's 3D formulation, but the problem is limited to 2 dimensions to limit computational time. The far field boundary is at 150 chords distance to damp unwanted reflections there. Simulations are run on the VEGA high-performance computing (HPC) cluster at Embry-Riddle Aeronautical University, Daytona Beach Campus. On 144 cores, the solution advances at ~0.6 seconds per day when $U_\infty = 7\ \mathrm{m{\cdot}s^{-1}}$ and $\Delta t = 30.86\cdot10^{-6}$ sec. Figure 2.1 shows the nearfield airfoil grid and detail of the rounded trailing edge (TE).

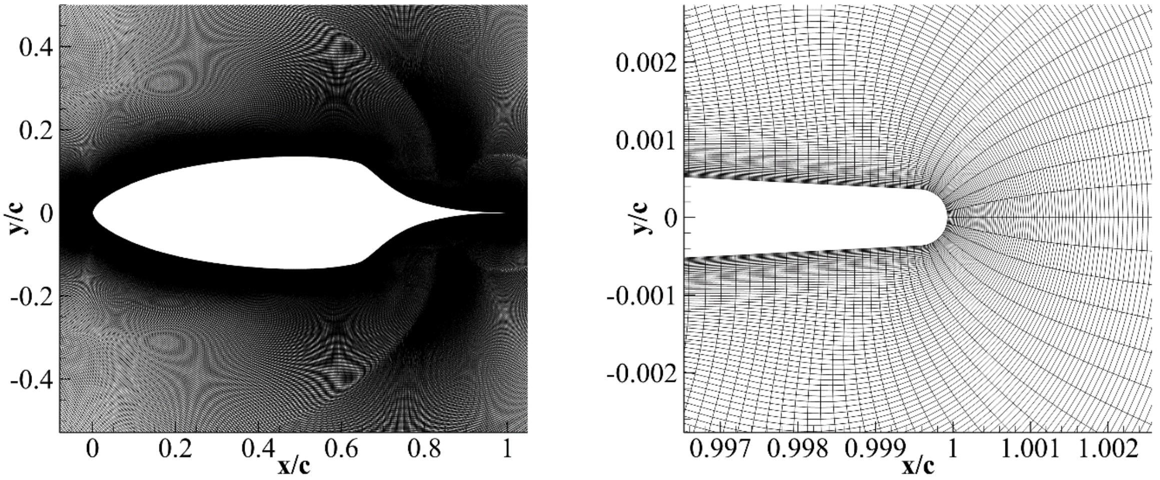

Figure 2.1: Computational grid used for FDL3DI near airfoil (left), and detail of TE (right).

FDL3DI is used for reliable, if expensive, simulations of uncontrolled LCO, however low-fidelity tools may be used for much of this work. Evaluating LCO control using SJAs is where the high-fidelity formulation is required. The required computational time is reduced by using FDL3DI for SJA optimization (position, size, velocity amplitude, frequency) and using the resulting control forces to apply control to the low-fidelity model.

2.2. Low-Fidelity Solver

For a low-fidelity flow solution, XFOIL is employed. XFOIL [24] is a potential panel method code for 2D analysis of generated NACA series airfoils or arbitrary input airfoils. Viscous effects are treated with integral boundary layer corrections and e^n free or specified fixed transition models. Flow solutions are found in minutes for a range of angles of attack (AoAs). The resulting lift and moment curves can be linked with the aeroelastic model to complete the low-fidelity LCO model.

The low fidelity tool allows rapid iteration on optimizing airfoil geometries for maximum LCO amplitude with minimum freestream velocity. This could be done manually or include XFOIL's full- and mixed-inverse design routines. Evaluations of control schemes can also utilize the low fidelity tool, provided high-fidelity or experimental data is available to generate the control authority.

If lift and moment are known, the aeroelastic model, Section 2.3, can be readily solved iteratively over time with a Runge-Kutta (RK4) scheme. Inputs into the prediction are the lift curve, which can be the result of experimental, high-, or low-fidelity data.

2.3. Aeroelastic Model

The linear, 2D aeroelastic model presented by Berggren [25] is implemented in both the high- and low-fidelity solvers to determine the pitching and plunging response of the airfoil:

$$M_S\ddot{p} + C_S\dot{p} + F(p)p = \begin{bmatrix} -lift \\ moment \end{bmatrix} \tag{2.1}$$

Where $p(t)$ is the state vector of plunging (h, meters) and pitching (α, radians):

$$p = \begin{bmatrix} h \\ \alpha \end{bmatrix} \tag{2.2}$$

The structural mass and damping coefficient matrices, M_S and C_S respectively are:

$$M_S = \begin{bmatrix} m & S_\alpha \\ S_\alpha & I_\alpha \end{bmatrix} \tag{2.3}$$

$$C_S = \begin{bmatrix} \zeta_h\sqrt{k_h m} & 0 \\ 0 & \zeta_\alpha\sqrt{k_\alpha I_\alpha} \end{bmatrix} \tag{2.4}$$

Where m, S_α, and I_α are the mass, static moment, and moment of inertia. The damping logarithm decrements of plunging and pitching are ζ_h and ζ_α, respectively. Linear stiffness coefficients are represented by k_h and k_α for plunging and pitching. The stiffness matrix also includes a cubic stiffness term for angle of attack:

$$F(p) = \begin{bmatrix} k_h & 0 \\ 0 & k_\alpha + k_{\alpha,3}\alpha^3 \end{bmatrix} \tag{2.5}$$

When linked with the numerical flow solutions, lift and moment are found from integrating pressure over the airfoil surface; the resulting force is substituted into the right-hand side of the equation. FDL3DI solves the resulting motion implicitly, using sub iterations to converge the flow and aeroelastic solutions before advancing time. The low-fidelity tool will implement a similar scheme.

2.4. Experimental Set-up

Experimental data was provided by Oksana Stalnov, Ron Efrati and Shay Monat, Technion-Israel Institute of Technology. The wind tunnel used was of closed return type, with a cross section of 0.5 m squared and 5.76:1. Static pressure was measured from 29 static pressure ports on both surfaces of the airfoil, shown in Figure 2.2, using HCLA series pressure transducers read by 24-bit data acquisition cards in a National Instruments (NI) PXIe-1082 chassis.

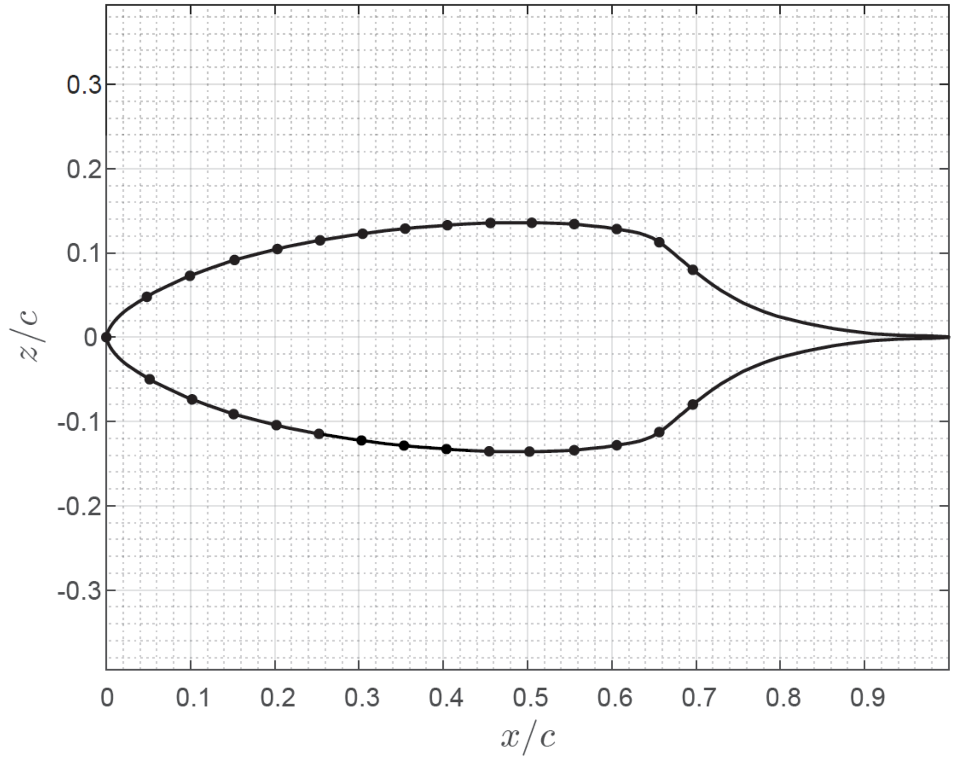

Figure 2.2 Modified Glauert airfoil with locations of experimental static pressure ports.

2.5. Power Prediction

To evaluate the potential of the concept for wind energy harvesting, some method is required for predicting the available energy of the wind and input control energy to find the net total energy. Beginning with the available flow power, defined by the kinetic energy of the incoming flow tube:

$$P_{avail} = \frac{1}{2}\rho U^3 A \tag{2.6}$$

Where P_{avail} is the power of the incoming flow, ρ atmospheric density, U wind velocity, and A area swept by the fluttering airfoil. Energy extracted by the harvester must reduce the flow velocity of the outlet, requiring a larger area for mass to be conserved across the device. Due to this, for rotating wind turbines, the Betz limit, $16/27$, is the maximum efficiency of output electrical power compared to input flow energy, although flutter-based wind energy harvesters have much lower efficiencies [26]. Thus, the net power generation can be given by:

$$P_{net} = \eta P_{avial} - P_{ctrl} = \eta_{mech}\eta_{piezo}\eta_{elec}P_{avail} - P_{ctrl} \tag{2.7}$$

Where the efficiency, η, could be expressed as the product mechanical, piezo, and electrical conversion efficiencies for more detailed design, and P_{ctrl} is the required power of the SJAs, if utilized to excite LCO.

Control power is predicted from the energy of the SJAs jet and an efficiency value. Since the SJA output is sinusoidal, its instantaneous power is also periodic:

$$P_{jet}(t) = \eta_{SJA}^{-1} \cdot \frac{1}{2}\rho\big(U_{SJA,max} \cdot \sin(\omega t)\big)^3 A_{SJA} \tag{2.8}$$

The function is integrated over one-half cycle to find the average value of jet power:

$$P_{jet} = \eta_{SJA}^{-1} \cdot \frac{1}{2}\rho U_{SJA,max} \cdot 2f \int_0^{\frac{1}{2f}} \sin^3(2\pi f t)\, dt \;\; A_{SJA} \tag{2.9}$$

$$P_{jet} = \eta_{SJA}^{-1} \cdot \frac{2}{3\pi}\rho U_{SJA,max}^3 A_{SJA} \tag{2.10}$$

3 Results

Steady state pressure distributions and lift curves were used to verify the high- and low-fidelity models against each other and validate them versus experimental results. High fidelity aeroelastic results are presented for 7 m·s^{-1} freestream velocity for various cases: uncontrolled, open loop pitch control, open loop plunge control, and closed loop plunge control. The plunge control cases are considered with 1 (plunging) and 2 (pitching and plunging) degrees of freedom.

3.1. Steady State Results

Steady state pressure distribution was used to compare both solvers to experimental data. Cases were run at 0° to 10° AoA in 2° steps, at the conditions shown in Table 3.1.

Table 3.1 Steady state experimental and numerical conditions.

Parameter	**Value**
Freestream velocity	12 m·s^{-1}
Atmospheric density	1.14 kg·m^{-3}
Atmospheric pressure	98 kPa
Reynolds number	180,000
Atmospheric viscosity	1.841·10^{-5} Pa·s
Atmospheric temperature	299 K

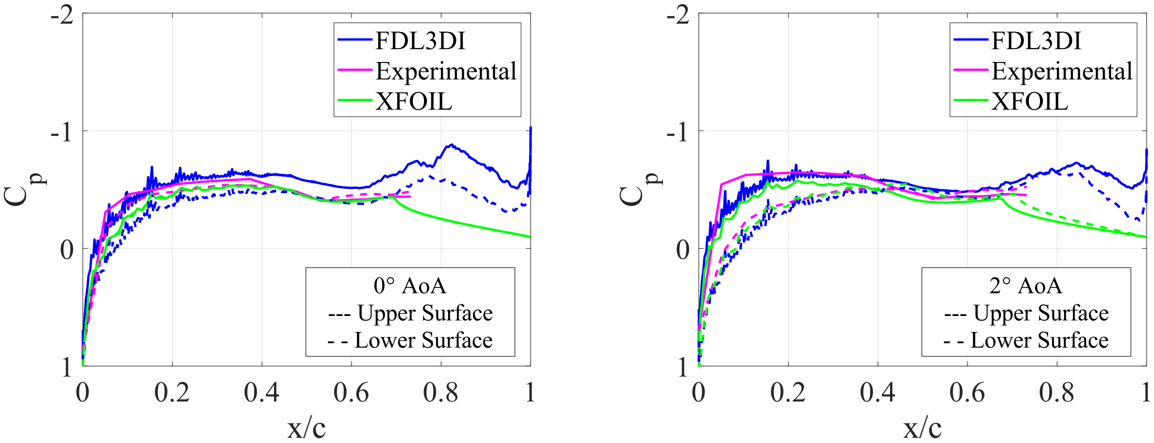

Figure 3.1 Steady state pressure distribution for 0° AoA (left) and 2° AoA (right).

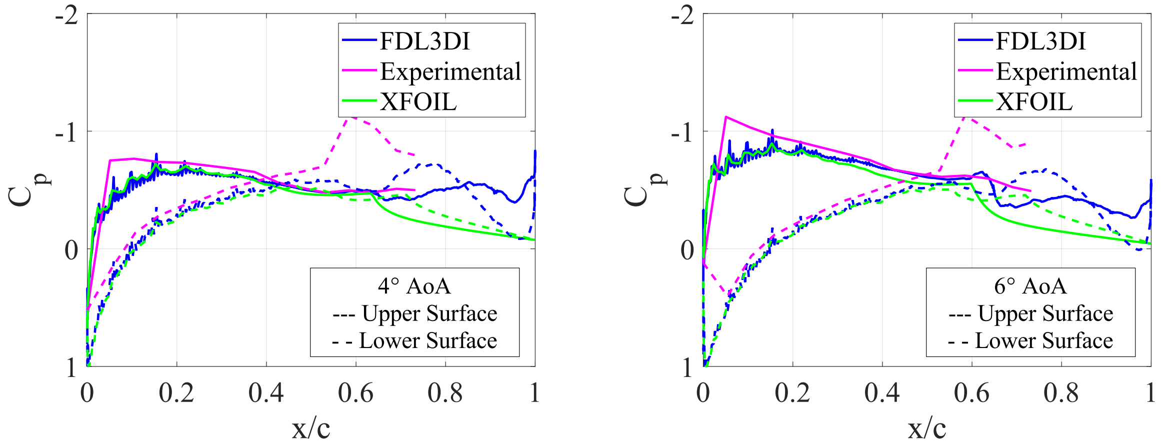

Figure 3.2 Steady state pressure distribution for 4° AoA (left) and 6° AoA (right).

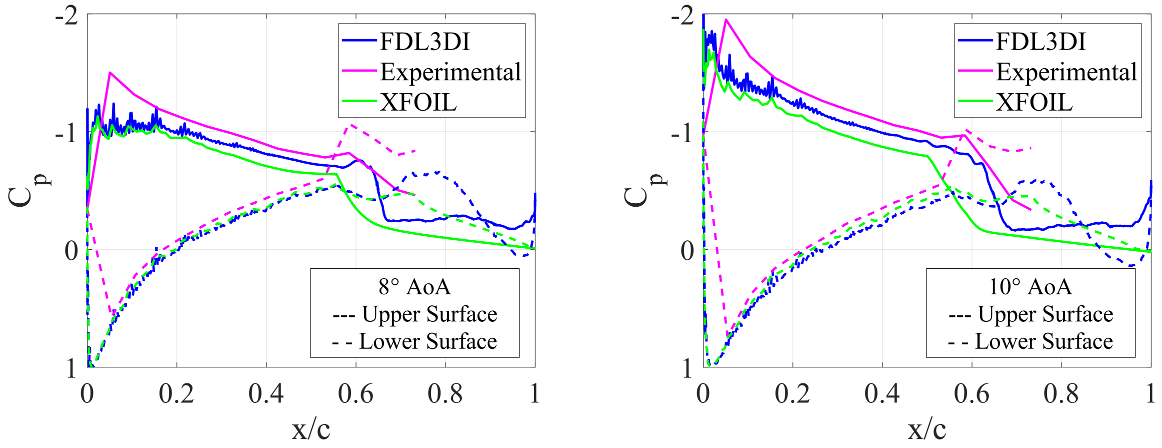

Figure 3.3 Steady state pressure distribution for 8° AoA (left) and 10° AoA (right).

Comparisons of steady state pressure distributions are shown in Figure 3.1, Figure 3.2, and Figure 3.3. Experimental results (magenta) are as expected from the leading edge (LE) to mid-chord, albeit with poor resolution near the LE. First comparing FDL3DI results (blue) to experiment, general agreement exists. Near the LE on the upper surface, FDL3DI tends to show a somewhat higher minimum pressure and place its position forward of the experimental result (noting of course the resolution limit of the experimental data near the LE). Experimental data exist up until 70% chord, just aft of the separation point, and FDL3DI agrees with experiment on the location of separation. On the lower surface at higher angles of attack (≥ 4° AoA) FDL3DI predicts separation from 60% chord, where the lower surface pressure in the experimental data shows lower pressure from the flow accelerating around the corner starting around 60% chord. Noise in the FDL3DI pressure distributions is an artifact from linear interpolation used to generate points for the computation grid used by FDL3DI in between points defining the airfoil geometry.

Moving to comparing XFOIL results (green) with experimental data, from the LE to mid-chord XFOIL closely matches FDL3DI results. Near the separation point, XFOIL successfully predicts the separation point, however it overpredicts pressure in the separated region, especially at lower AoAs. Overall, XFOIL is a useful tool for this flow configuration, especially considering the 3 orders of magnitude of difference in execution time.

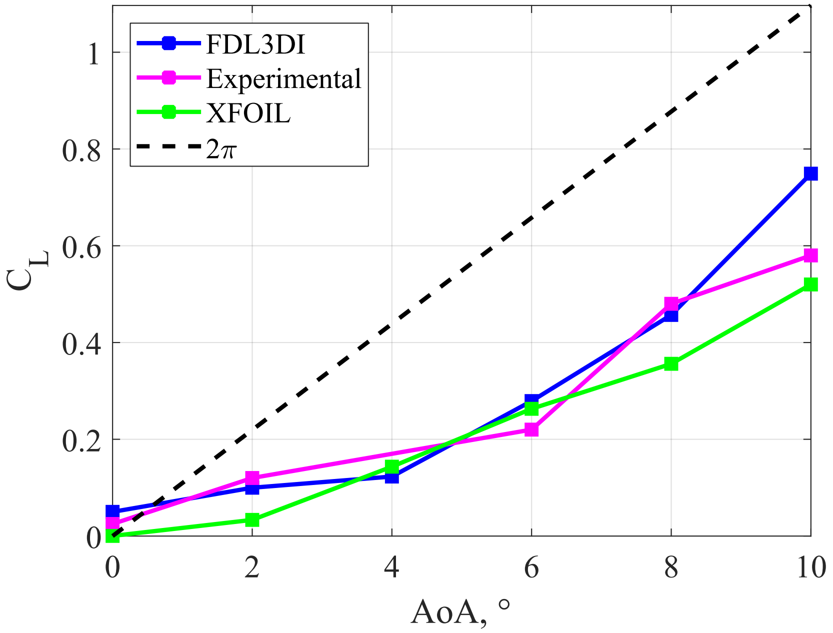

Figure 3.4 Lift curve comparison between numerical, experimental, and thin airfoil theory results.

Integrating pressure to find lift, the resulting lift curves are shown in Figure 3.4. The airfoil is subcritical by all estimations, with a lift curve slope below the predicted value of inviscid thin airfoil theory, 2π. Both numerical methods begin to capture nonlinearity in the lift curve as the separation on the lower surface reduced with AoA increase.

3.2. Uncontrolled Aeroelastic Results

The aeroelastic response of the airfoil is first considered without control, with a freestream velocity of 7 $\text{m}\cdot\text{s}^{-1}$ and subcritical Reynolds number of 104,200. Structural parameters, shown in Table 3.2, are matched to values employed by Berggren [25]. 2-DOF motion is simulated to match with previous results and the canonical Theodorsen problem from unsteady thin airfoil theory. As shown in Figure 3.5, with 2-DOF a plunging LCO of up to 0.2 chords is present at a freestream velocity below the classically predicted critical flutter velocity. Comparing the pitching and plunging motion over time, the two degrees of freedom do not couple at this velocity, with a fundamental pitching frequency of 4.51 Hz and plunging frequency of 1.01 Hz. Combined with the third major frequency present in the flow, the shedding frequency of vortices from the separated regions of flow near the airfoil, plunging LCO is not constant and there is a fluctuation of amplitude between each cycle.

Table 3.2 structural parameters considered for aeroelastic response [25].

$\rho = 1.1\,kg/m^3$	$b = 0.11\,m$	$a = -0.024\,m$
$m = 2.55\,kg$	$a_1 = 0.165$	$a_2 = 0.0455$
$S_\alpha = 1.04\times10^{-2}\,kg\cdot m$	$b_1 = 0.335$	$b_2 = 0.300$
$I_\alpha = 2.51\times10^{-3}\,kg\cdot m$	$k_\alpha = 9.3\,N/m$	$k_{\alpha^3} = 55\,N/m$
$k_h = 450\,N/m$	$\zeta_h = 5.5\times10^{-3}$	$\zeta_\alpha = 1.8\times10^{-2}$

1-DOF aeroelastic LCO was studied for two reasons: it is a purely viscous phenomena as it is not predicted by classical inviscid theory, and it may allow for a simpler and more cost-effective structure of a wind energy harvester. The 1-DOF aeroelastic response is shown alongside the 2-DOF response in Figure 3.5, and shows similar maximum plunging amplitude of 0.2 chords despite one less degree of freedom. This confirms that in this velocity regime the combination of uncoupled pitching and plunging along with the low amplitude of pitching, ≥1°, the response of the airfoil is focused on separation affecting lift, not moment.

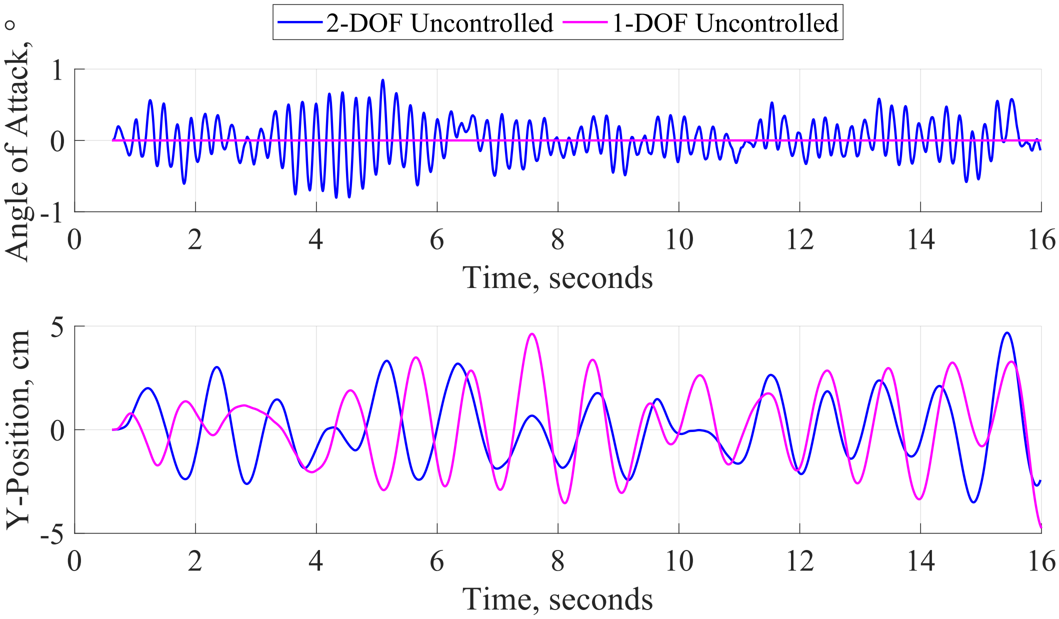

Figure 3.5 Uncontrolled aeroelastic response at 7 m·s^{-1} with 1- and 2-DOF.

3.3. Synthetic Jet Actuation (SJA) Response

To increase the plunging LCO amplitude and energy harvesting potential, SJAs are considered as an actuator gaining control authority by controlling separation. The SJA are treated as a sinusoidal velocity boundary condition having an amplitude of 13.5 m·s^{-1} and frequency of 200 Hz:

$$U_{SJA} = U_{SJAmax} \sin(\omega_{SJA} t) \qquad (3.1)$$

SJAs are embedded in the airfoil surface at 68% chord just aft of the separation point for maximum potential to affect the flow, as shown in Figure 1.7. The geometry of the MG airfoil, with large, separated regions downstream of the SJA locations, increased the domain of influence of the SJAs, thus increasing their control authority. Time averaged pressure contours are shown for static airfoils with an SJA active on the upper surface and with no control in Figure 3.7. As the airfoil is at 0° AoA, the separation on the upper and lower surface of the uncontrolled airfoil (left) is symmetrical. With the upper surface SJA active (right), the recirculation is reduced and thus pressure increased in that region. The resulting pressure distributions are shown in Figure 3.6.

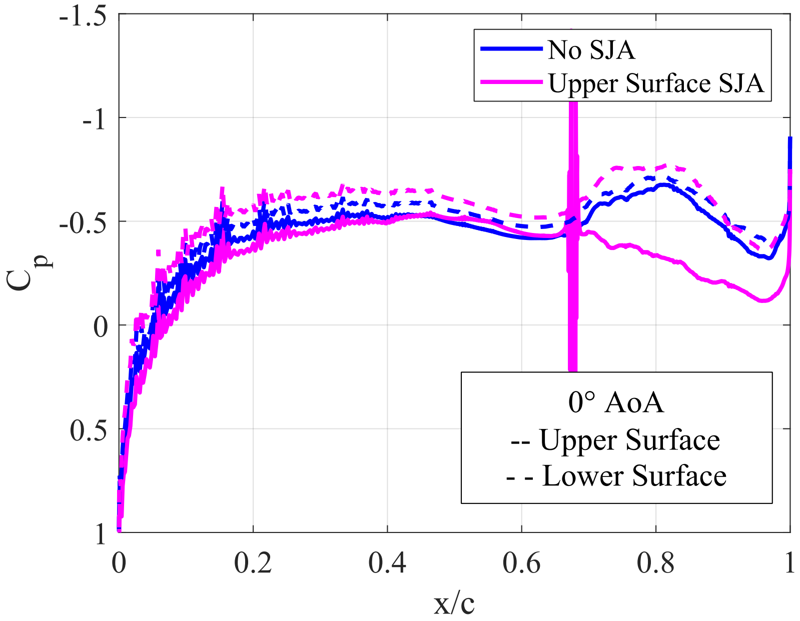

Figure 3.6 Surface pressure distribution on an MG airfoil without (blue) and with (magenta) SJA active on the upper surface at 68% chord.

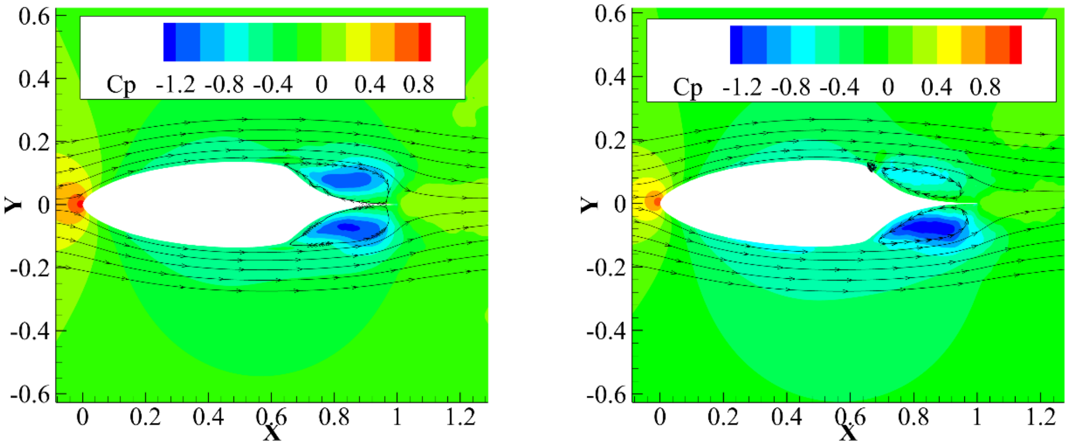

Figure 3.7 Pressure contours around a fixed airfoil without (left) and with (right) an SJA active on the upper surface, showing the SJA's flow reattachment effect. Streamlines highlight the size of the recirculating regions.

The resulting increase of surface pressure on the upper surface decreases the lift and increased the moment (airfoil tends to increase angle of attack). Put another way, the airfoil would tend to plunge away from the active SJA and pitch toward the active SJA. The behavior of lift coefficient and moment coefficient over time is shown in Figure 3.8.

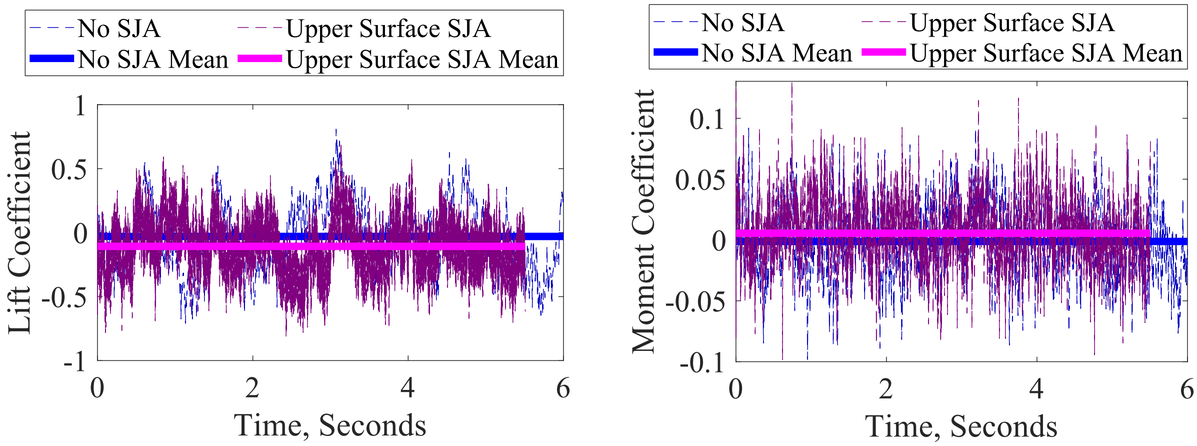

Figure 3.8 Lift coefficient (left) and moment coefficient (right) behavior of an MG airfoil with an SJA active on the upper surface, compared to an uncontrolled airfoil.

3.4. Controlled Pitch Following Aeroelastic Results

Utilizing the embedded SJAs to demonstrate their effectiveness, one SJA is always active, and the controller switches between the SJA on each surface. Open-loop control is considered first as the simplest case, here switching with the pitching fundamental frequency. For comparison and to ensure that the control input is phase-locked to the airfoil motion, a simple closed-loop controller is considered. Observing the airfoil motion in pitching, the upper surface SJA is active when AoA is increasing, and the lower surface SJA is active when AoA is decreasing.

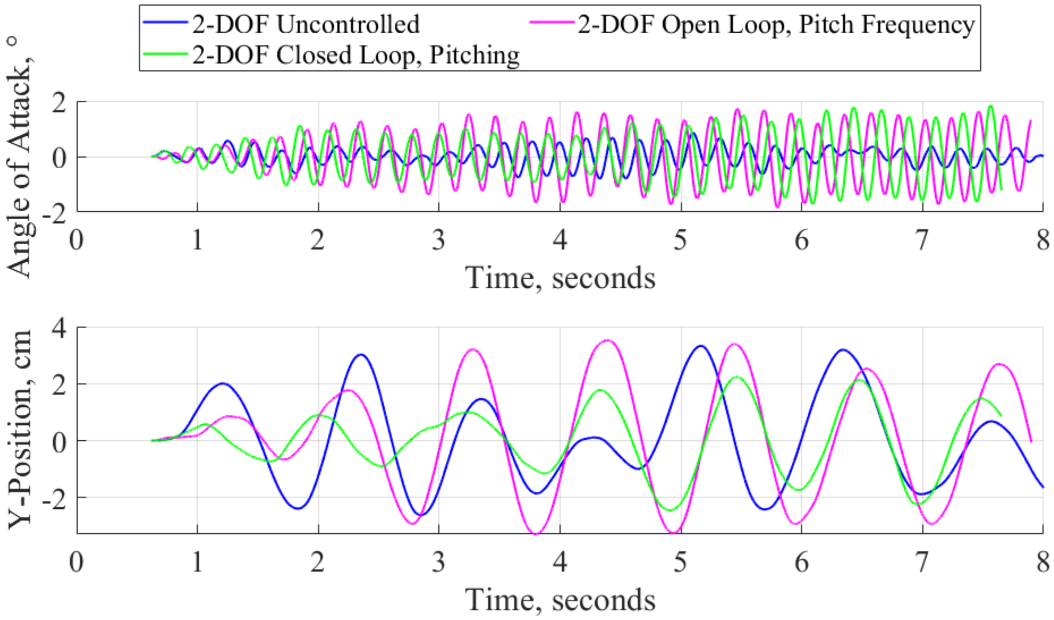

Figure 3.9 LCO Response of MG airfoil under open-loop (magenta) control with the pitching fundamental frequency and closed-loop (green) pitch following control compared with the uncontrolled (blue) response.

The response to both controllers is shown in Figure 3.9 along with the uncontrolled response. Both controllers increase the pitching LCO amplitude from ~1° to ~2° maximum. In addition, the LCO amplitude has been regularized, so that the average amplitude of each cycle is closer to the maximum seen over the time tested. While demonstrating the general authority of SJAs in this configuration and the capability to amplify LCO motion, pitching LCO is less useful for harvesting wind energy, which utilizes plunging motion. The effect on plunging amplitude of controlling following pitching is minimal. However, the plunging amplitude is regularized, especially by the open-loop controller.

3.5. Controlled Plunge Following Aeroelastic Response

Toward the direct goal of increasing wind energy harvesting potential from a device utilizing plunging LCO, similar open- and closed-loop controllers are implemented with respect to plunging. In this case, for closed-loop control, the lower SJA is activated when the airfoil is plunging upward to increase the amplitude of motion. The controlled and uncontrolled cases are shown in Figure 3.10. Both controllers are able to increase the plunging amplitude from ~0.2 chords to ~ 0.35 chords and regularize the plunging LCO.

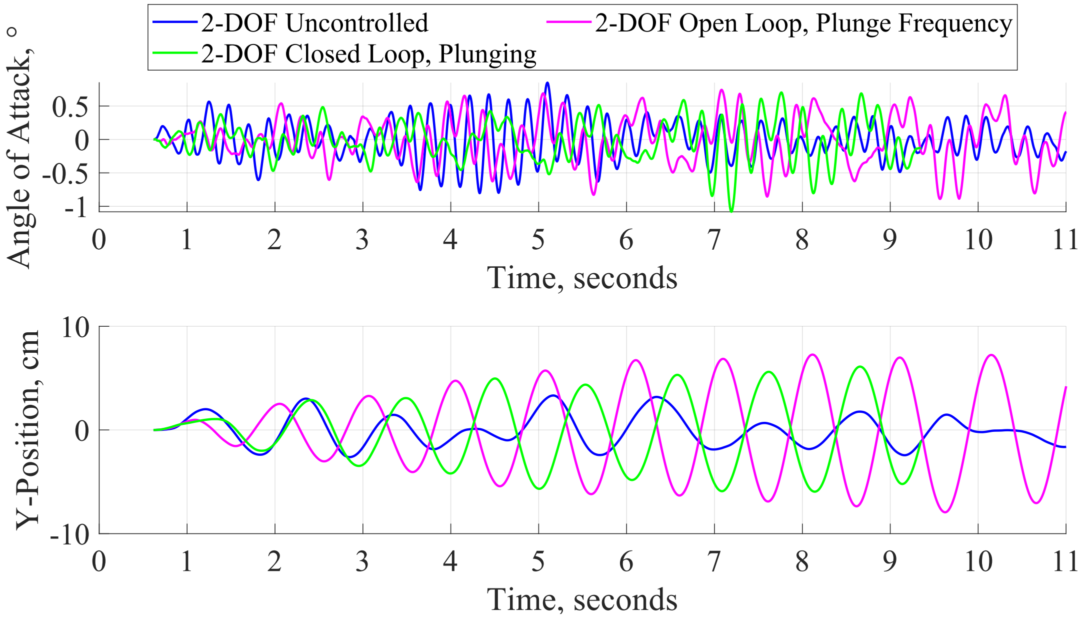

Figure 3.10 Response of MG airfoil under open-loop (magenta) control with the plunging fundamental frequency and closed-loop (green) plunge following control compared with the uncontrolled (blue) response, 2-DOF.

Now with control, pitch and plunge begin to couple, as shown in Figure 3.11. Pitching motion consists of two major frequencies added together: a lower amplitude natural pitching frequency and higher amplitude natural plunging frequency. The mean motion of AoA is now phase locked to the plunging motion. When the airfoil is plunging away from the neutral axis, it is also pitched away, so AoA is helping to increase plunging amplitude. The inverse is true when the airfoil is plunging toward the neutral axis. Thus, the effect of the pitching degree of freedom on one half of a plunge cycle counteracts the effect on the other half. Interestingly, after 7 seconds, the pitching oscillation falls in to a 2.5:1 resonance with the plunging motion (and as this is closed-loop SJA activity), increasing the minor oscillation in pitch around the main LCO.

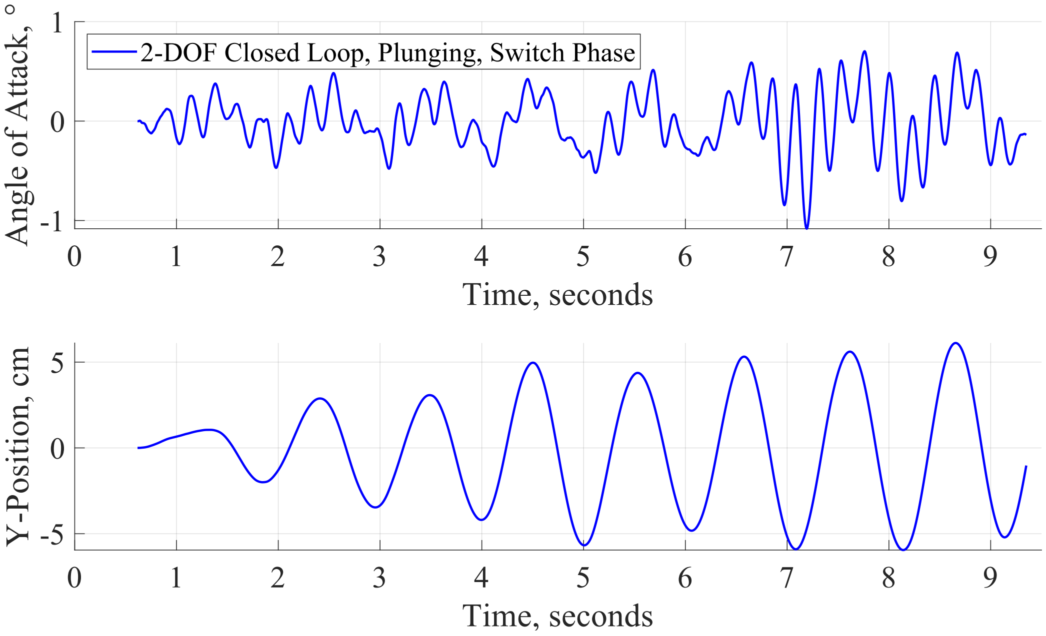

Figure 3.11 2-DOF closed-loop plunge following control response to detail coupling between AoA and plunging.

Reducing the problem to 1-DOF in the plunging direction, in Figure 3.12, the controlled cases are compared to 1-DOF plunging motion. Here, the 1-DOF closed-loop controller shows similar behavior as seen with 2-DOF, plunging amplitude increased to ~0.35 chords and regularization. The open-loop 1-DOF case failed to couple the control input with the resulting motion, as shown in Figure 3.13, so the plunging excitation was minimal.

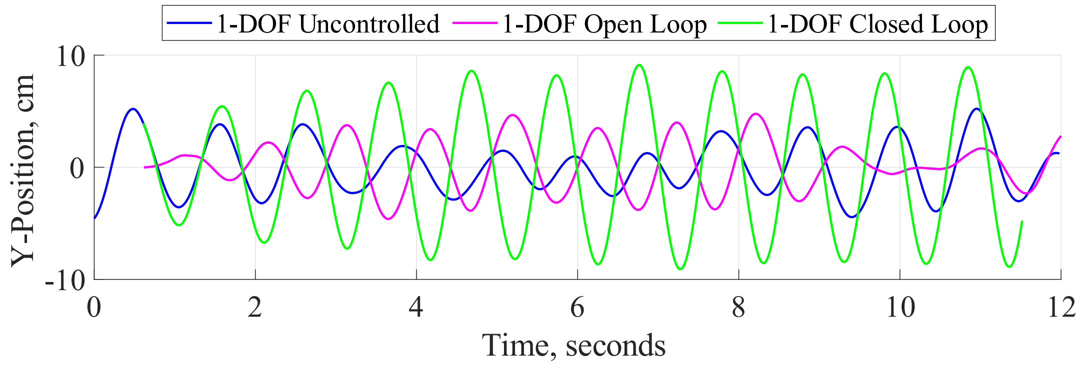

Figure 3.12 Response of MG airfoil under open-loop (magenta) control with the plunging fundamental frequency and closed-loop (green) plunge following control compared with the uncontrolled (blue) response, 1-DOF.

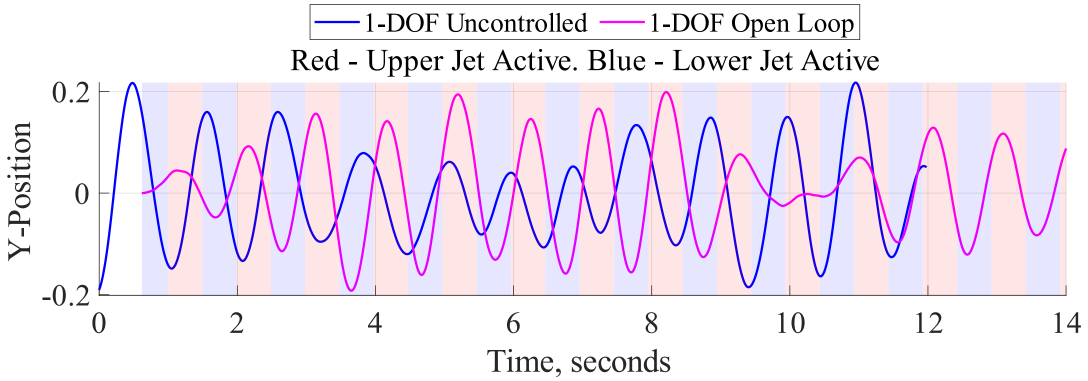

Figure 3.13 1-DOF open-loop control (magenta) with shading indicating SJA activity. The plunging response failed to couple to the control input, so plunging excitation is minimal.

The highest amplitude plunging cases, 2-DOF open-loop plunging frequency and 1-DOF closed-loop, are compared in Figure 3.14. Both cases achieve similar maximum plunging amplitude despite the different degrees of freedom. At these subcritical velocities, the extra pitching degree of freedom does little to enhance plunging LCO.

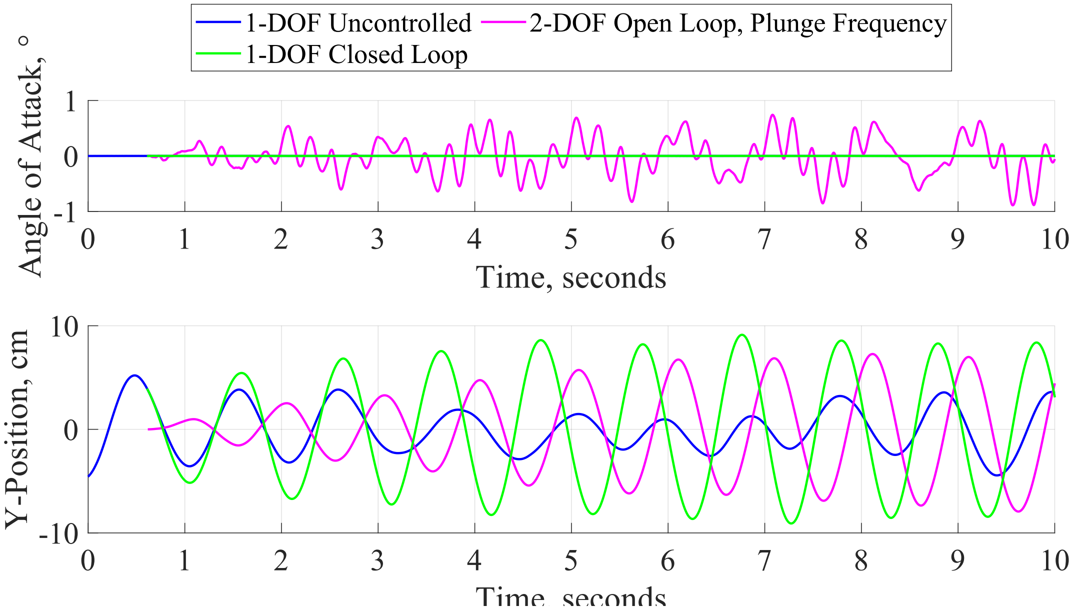

Figure 3.14 Comparison of 2-DOF open-loop plunging frequency (magenta) and 1-DOF closed-loop control (green) with 1-DOF uncontrolled (blue) response.

3.6. Low-Fidelity Method Verification

To verify the low-fidelity model, data from FDL3DI is fed into the model and compared to the output low-fidelity results. The first point of verification is the RK4 scheme. FDL3DI data (such as position and forces/moments over time) are used as input to the aeroelastic model solved with RK4, and the resulting airfoil motion shown in Figure 3.15. With the correct heaving stiffness, 450 N/m, the low-fidelity model greatly underpredicts amplitude of plunging motion. Adjusting the heaving stiffness to 100 N/m for the model produces good agreement between the two solvers. Future work will continue to improve the agreement between the high- and low-fidelity models, to facilitate the rapid optimization of the system.

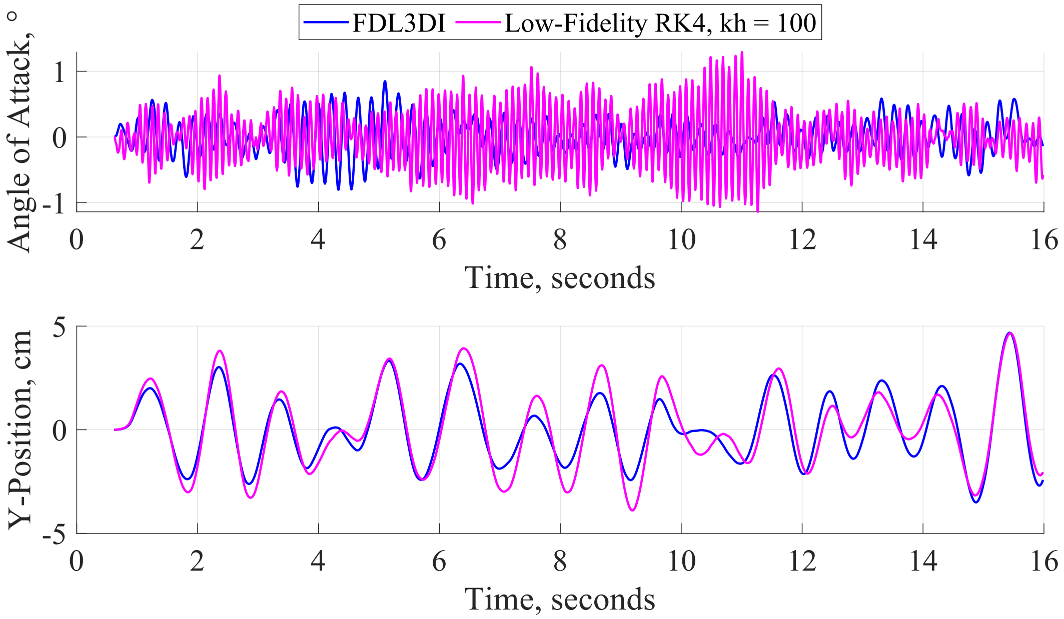

Figure 3.15 Verification of Low order RK4 aeroelastic solver with FDL3DI high-fidelity input.

3.7. Power Prediction

Using the formulation of Section 2.5, (2.6 is used to find the available power to the wind energy harvester, based on the area swept through plunging motion and 1 meter span. Equation (2.10 is used to estimate the power required for SJA control, based on an SJA being active 100 % of the time, when control is active. Together, the power available and control power are input to Equation (2.7 along with the required efficiencies to estimate the net power available for use. Both uncontrolled cases had an average peak to peak displacement of ~0.25 chord (6 cm) compared to the ~0.6 chord (14.4 cm) given a chord of 0.24 m. for the controlled case, the SJA is considered as a slot 0.05 chord (1.2 mm) wide along the entire span, and SJA parameters are shown in Table 3.3. overall, the SJA uses 1.43 W to excite a meter span of airfoil, based on an efficiency of 45%, as demonstrated by Feero et. al [27] for a circular SJA with a 2 mm orifice and peak velocity of 15 m/s. Table 3.4 shows the final power results for the best uncontrolled and controlled cases. Without control, the system produces net 2.35 W per meter span, which increased by 1.70 W to net 4.05 W for the controlled case, a 72.3% improvement assuming the system is 20% efficient at capturing the incoming flow kinetic energy.

Table 3.3 SJA performance parameters.

Parameter	**Value**
Jet width	1.2 mm
Jet efficiency	0.5
Jet maximum velocity	13.5 m/s
Power required per meter span	1.59 W

Table 3.4 Power prediction from high-fidelity simulation of MG airfoil flutter.

Parameter	**Value**	
	Uncontrolled	**Controlled**
Peak to peak plunging	6 cm	14.4 cm
Available power per meter span	2.35 W	5.64 W
Control power per meter span	0 W	1.59 W
Net power per meter span	2.35 W	4.05 W
% difference to uncontrolled	-	72.3%
Chord	24 cm	
Freestream velocity	7 m/s	
Atmospheric density	1.142 kg/m^3	
Efficiency	0.2	

4 Conclusions

The high-fidelity ILES code FDL3DI was validated against steady state experimental data. And the low-fidelity panel method code XFOIL was validated against steady state experimental data and compares well with FDL3DI. The quasi-linear aeroelastic model from Berggren was implemented into FDLDI.

2-DOF LCO exists below the classical critical flutter velocity, helped by flow separation from the MG airfoil. 1-DOF LCO exists, unlike in classical inviscid flutter prediction, due to separation around the MG airfoil. It is of similar plunging amplitude to 2-DOF motion. This could lead to a simpler mechanical design as there is only 1 motion path, and it is linear not rotational.

SJAs embedded in the MG airfoil affect the flow separation. An active SJA on the upper surface produces a lift plunging the airfoil downward and a moment pitching the airfoil upward.

Exciting the 2-DOF system in the pitching frequency excites the pitching LCO but has little effect on plunging LCO (plunging LCO is to be utilized to harvest wind energy). Both 1- and 2-DOF cases when excited with the plunging frequency increased plunging amplitude. Open-loop control can be effective to demonstrate the concept, but generally the control falls out of phase with the response causing plunging amplitude to remain lower. A simple-closed loop controller locking the control input to plunging motion allows the control to continue to increase plunging amplitude.

The power produced by the system was estimated to be 2.35 W without SJA control increasing to 4.05 W per meter span with SJA control at 7 m/s wind speed. While overall power output is low, all aspects of the design are still to be optimized to increase power output, such as airfoil geometry, structural parameters, and SJA placement and operation.

The aeroelastic model was solved with RK4 and compared to FDL3DI results. With an adjusted heaving spring constant, the two models of airfoil motion can be brought into agreement. The lower order model will continue to be investigated to improve its agreement with the high-fidelity FDL3DI results, so as to allow the low order tool to reduce development time in analyzing new airfoil geometries and structural parameters.

Future work would focus on first finalizing the low order model and bringing the spring constants into agreement. Then SJA control can be implemented, such as by way of force added as based on FDL3DI steady state SJA simulations. The other sources of lift curve (experiment and XFOIL) are also to be validated as to their effect on airfoil motion.

Work would then move to optimization of the system for maximum energy harvesting potential. FDL3DI use could be limited to validation cases, and optimization of SJA position and operation parameters. XFOIL would be used to rapidly evaluate airfoil geometries, along with the low order aeroelastic model to determine the resulting LCO. The low order model is useful to optimize control schemes and structural parameters as well.

REFERENCES

[1] Wiser, R., Bolinger, M., Hoen, B., Millstein, D., Rand, J., Barbose, G., Darghouth, N., Gorman, W., Jeong, S., O'Shaughnessy, E., and Paulos, B., "Land-Based Wind Market Report: 2023 Edition," United States Department of Energy Office of Energy Efficiency & Renewable Energy, 2023.

[2] Fung, Y. C., "An Introduction to the Theory of Aeroelasticity," Dover Publications, Inc., Garden City, New York, 2008.

[3] Straganac, T. W. and Mook, D. T., "Numerical Model of Unsteady Subsonic Aeroelastic Behavior," *AIAA Journal*, Vol. 28 No. 5, May 1990, pp. 903-909. https://doi.org/10.2514/3.25137

[4] Abbott, I. H., Von Doenhoff, A. E., and Stivers Jr., L. S., "Report No. 824: Summary of Airfoil Data," National Advisory Committee for Aeronautics, Washington D.C., 1945.

[5] Van Valkenburg, M. E. and Middleton, W. M., "Reference Data for Engineers: Radio, Electronics, Computers, and Communications," 9th ed., Newnes, Boston, 2002, pp 15-23–15-24.

[6] Nabavi, S. and Zhang, L., "Portable Wind Energy Harvesters for Low-Power Applications: A Survey," *Sensors*, Vol. 16, MDPI, 2016. https://doi.org/10.3390/s16071101

[7] Li, Z., Zhou, S., and Yang, Z., "Recent Progress on Flutter-based Wind Energy Harvesting," *International Journal of Mechanical System Dynamics*, No 2. Wiley, 2022, pp. 82-89. https://doi.org/10.1002/msd2.12035

[8] Ma, X. and Zhou, S., "A Review of Flow-Induced Vibration Energy Harvesters," *Energy Conversion and Management*, Vol. 254, Elsevier, 2022. https://doi.org/10.1016/j.enconman.2022.115223

[9] Lu, Z., Wen, Q., He, X., and Wen, Q., “A Flutter-Based Electromagnetic Wind Energy Harvester: Theory and Experiments,” *Applied Sciences*, Vol. 9, MDPI, 2019.

https://doi.org/10.3390/app9224823

[10] Safei, M., Sodano, H. A., and Anton, S. R., “A Review of Energy Harvesting Using Piezoelectric Materials: State-of-the-art a Decade Later (2008-2018),” *Smart Materials and Structures*, Vol. 28, IOP Publishing, 2019.

https://doi.org/10.1088/1361-665X/ab36e4

[11] Bae, J., Lee, J., Kim, S., Ha, J., Lee, B., Park, Y., Choong, C., Kim, J., Wang, Z., Kim, H., Park, J., and Chung, U., “Flutter-Driven Triboelectrification for Harvesting Wind Energy,” *Nature Communications*, Vol. 5., Macmillan Publishers Limited, 2014.

https://doi.org/10.1038/ncomms5929

[12] Xia, Y., Tian, Y., Zhang, L., Ma, Z., Dai, H., Meng, B., and Peng, Z., “An Optimized Flutter-driven Triboelectric Nanogenerator with a Low Cut-in Wind Speed,” *Micromachines*, Vol. 12., MDPI, 2021.

https://doi.org/10.3390/mi12040366

[13] Glauert, M. B., “Aeronautical Research Council Reports and Memoranda No. 2111: The Design of Suction Aerofoils with a Very Large C_L-Range,” Aeronautical Research Council, London, November 1945.

[14] Glauert, M. B., “Aeronautical Research Council Reports and Memoranda No. 2683: The Application of the Exact Method of Aerofoil Design,”, Aeronautical Research Council, London, October 1947.

[15] Lighthill, M. J., “Aeronautical Research Council Reports and Memoranda No. 2112: A New Method of Two-dimensional Aerodynamic Design,” Aeronautical Research Council, April 1945.

[16] Goldschmied, F., “Thick-Wing Spanloader All-Freighter: Design, Concept for Tomorrow’s air Cargo,” *AIAA/AHS/ASEE Aircraft Design, Systems and Operations Conference Paper 90-3198*, Dayton, Ohio, September 17-19, 1990.

https://doi.org/10.2514/6.1990-3198

[17] Saeed, F., and Selig, M. S., “Multipoint Inverse Airfoil Design Method for Slot-Suction Airfoils,” *Journal of Aircraft*, Vol. 33, No.4, July-August 1996.

https://doi.org/10.2514/3.47005

[18] Seifert, A., and Pack, L. G., “Active Flow Separation Control on Wall-Mounted Hump at High Reynolds Numbers,” *AIAA Journal*, Vol. 40, No. 7, July 2002.

https://doi.org/10.2514/2.1796

[19] Yom-Tov, J., and Seifert, A., “Multiple Actuators Flow Control over a Glauert-Goldschmied type Airfoil at Low Reynolds Numbers,” *35th AIAA Fluid Dynamics Conference and Exhibit paper 2005-5389*, Toronto, Ontario Canada, 6-9 June 2005.

https://doi.org/10.2514/6.2005-5389

[20] Seifert, A., Daivd, S., Stalnov, O., and Dayan, I., “Roll Control via Active Flow Control: From Concept to Flight,” *Journal of Aircraft*, Vol. 47., No. 3, May-June 2010.

https://doi.org/10.2514/1.45910

[21] Ja’fari, M., Shojae, F. J., and Jaworski, A. J., “Synthetic Jet Actuators: Overview and Applications,” *International Journal of Thermofluids*, Vol. 20, 2023.

https://doi.org/10.1016/j.ijft.2023.10043

[22] Tang, H. and Zhong, S., “Incompressible Flow Model of Synthetic Jet Actuators,” *AIAA Journal*, Vol. 44., No. 4, April 2006.

https://doi.org/10.2514/1.15633

[23] Gaitonde, D. V., and Visbal, M. R., "High-order schemes for Navier-Stokes equations: algorithms and implementation into FDL3DI," Air Force Research Laboratory, Wright-Patterson Air Force Base, Ohio, August 1998.

[24] Drela, M., "XFOIL: An Analysis and Design System for Low Reynolds Number Airfoils," *Conference on Low Reynolds Number Airfoil Aerodynamics,* University of Notre Dame, June 1989.

https://doi.org/10.1007/978-3-642-84010-4_1

[25] Berggren, D., "Investigation of limit cycle oscillations for a wing section with nonlinear stiffness," *Aerospace Science and Technology*, Vol. 8, 2004, pp. 27-34.

https://doi.org/10.1016/j.ast.2003.08.006

[26] Caracoglia, L., "Feasibility Assessment of a Leading-edge-flutter Wind Power Generator," *Journal of Wind Engineering and Industrial Aerodynamics*, Vol. 98, October-November 2010, pp. 679-686.

https://doi.org/10.1016/j.jweia.2010.04.006

[27] Feero, M. A., Lavoie, P., and Sullivan P. E., "Influence of Cavity Shape on Synthetic Jet Actuator," *Sensors and Actuators A: Physical*, Vol. 223, March 2015, pp. 1-10.

https://doi.org/10.1016/j.sna.2014.12.004